Quantum simulations of band-to-band tunnelling in a type-II broken-gap superlattice diode

Marcin Makowiec [ID], Andrzej Kolek[*][ID]

Department of Electronics Fundamentals, Rzeszow University of Technology, al. Powstańców Warszawy 12, Rzeszów 35-959, Poland

Article info	Abstract
	In recent years, type-II superlattice-based devices have completed the offer of the electronic industry in many areas of applications. Photodetection is one of them, especially in the mid-infrared wavelength range. It is due to the unique feature of a superlattice material, which is a tuneable bandgap. It is also believed that the dark current of superlattice-based photodetectors is strongly suppressed due to the suppression of the band-to-band tunnelling current in a superlattice material. This argument relies, however, on a semi-classical approach that treats superlattice as a bulk material with effective parameters extracted from the **k·p** analysis. In the paper, a superlattice device is analysed on a quantum level: the non-equilibrium Green's function method is applied to the two-band Hamiltonian of the InAs/GaSb superlattice p-i-n diode. The analysis concentrates on the band-to-band tunnelling with the aim to validate the correctness of a semi-classical description of the phenomenon. The results of calculations reveal that in a superlattice diode, the inter-band tunnelling occurs only for certain values of energy and in-plane momentum, for which electronic and hole sub-bands cross. The transitions occurring for vanishing in-plane momentum produce resonances in the current-voltage characteristics – the feature which was reported in a few experimental observations. This scenario is quite different from that occurring in bulk materials, where there is a range of energy-momentum pairs for which the band-to-band tunnelling takes place, and so current-voltage characteristics are free from any resonances. However, simulations show that, while not justified for a detailed analysis, the semi-classical description can be applied to superlattice-based devices for an 'order of magnitude' estimation of the band-to-band tunnelling current.

1. Introduction

Optoelectronic devices using a broken-gap type-II superlattice (T2SL) attract an immense and continuously growing interest. It concerns mainly devices operating in mid- and long-infrared wavelength and is due to the unique feature offered by a T2SL material, i.e., the possibility of flexible bandgap engineering in the respectiveenergy range. Additional advantages include excellent wafer uniformity (important for pixel matrices), high absorption coefficient, reduced Auger-type recombination, and reduced inter-band tunnelling current [1]. The arguments behind these state-ments are both theoretical and experimental. The former ones are usually based on the

semi-classical understanding of phenomena occurring in bulk materials. However, it is not always justified, especially for the phenomena of a purely quantum nature; Zener tunnelling is the first to mention, however, doubts may concern other basic components of the dark current resulting from diffusion, generation-recombination, and trap-assisted tunnelling (TAT) mechanisms because, classically, transport is forbidden in the barrier layers that form the superlattice (SL).

In this paper, the focus is on the inter-band tunnelling current, which in the devices devoted to mid-infrared (mid-IR) applications is mostly (due to the materials used for their growth) a direct band-to-band (btb) tunnelling current. The belief that it is significantly reduced in an SL material relies on a textbook description of this process [2] which relates the btb transmission coefficient:

*Corresponding author at: akoleknd@prz.edu.pl

$$T(E,k) = \exp\left(-\frac{4\sqrt{2m_r}E_g^{3/2}(E,k)}{3eFh}\right), \qquad (1)$$

at energy E, and in-plane wavevector k, to bandgap energy E_g, electric field F, electronic charge e, and reduced Planck constant $\hbar$. Apparently, equation (1) predicts a decrease of the transmission coefficient with an increase of the reduced mass, m_r. This mass is related to the effective masses of electrons and holes generated in the inter-band transition. The minibands formed in the SL material are much narrower than the bands in bulk materials, so the effective masses of the carriers travelling in the minibands are much larger. Therefore, tunnelling between the minibands, which depends exponentially on the parameter m_r, is supposed to be significantly reduced in SL materials [3–5]. The first step to assess this conjecture is to verify whether the semi-classical description applies to this quantum phenomenon. It can be done by comparing the results of semi-classical predictions and quantum analyses of electronic transport. As for the latter, the method used for this purpose should not only integrate coherent and incoherent processes but also could be effectively applied to real structures. One of few is the non-equilibrium Green's function (NEGF) formalism implemented in numerical simulations [6]. In the paper, this method has been used to answer the question raised above.

The NEGF method developed in the 1960s [7, 8] has only recently been used to analyse and/or model real electronic devices. It became possible (and necessary) due to (i) adaptation of the complex formalism into 'easy to implement' equations [9], (ii) intense growth of computational resources and development of numerical algorithms, both enabling the efficient use of the method, (iii) development of new devices whose operation relies on quantum phenomena. Consequently, in recent years, the NEGF method has been used for studying electronic transport phenomena in resonant tunnelling diodes [10], field effect [11] and tunnelling [12] transistors, carbon nanotube devices [13], light-emitting diodes [14–16], photodetectors [17–19], quantum-well solar cells [20–22], quantum [23–26] and inter-band [27] cascade lasers and, eventually, SL-based devices [28–31].

The inter-band tunnelling was accounted for in the number of NEGF-involved calculations [12, 29, 32], with only one devoted to the SL-based device [29]. The lack of more works is strongly influenced by the complexity of the method and a huge numerical load connected with this type of calculations. Therefore, similarly to many others [14, 20, 31, 33, 34], in the following sections of the paper, a p-i-n T2SL diode is modelled with a two-band Hamiltonian – the simplest that can account for inter-band tunnelling. The results of such calculations could shed some light on the concept of approximation, in which SL material is replaced by an equivalent bulk material. However, the conjecture about a significant reduction of the btb tunnelling current in SL devices can hardly be verified with this model.

This hypothesis was formulated for the SL devices, in which the tunnelling transition occurs between the first conduction (C1) and the first heavy-hole (HH1) miniband. Unfortunately, the HH1 band is not accounted for in a two-

band model. In Fig. 1, the dispersion relations calculated for 4-band and 2-band **k·p** Hamiltonians are compared. The former was calculated for a typical SL device devoted to mid-IR applications, which poses a bandgap of $\cong 0.2$ eV. In the 2-band model, a similar value of the bandgap between first conduction and first hole (H1) minibands can be obtained for much wider layers; the 6/6 nm SL period was assumed in order to fit the outcome from the 2-band model to a bandgap of 3.2/3.2 nm SL calculated with a 4-band model.
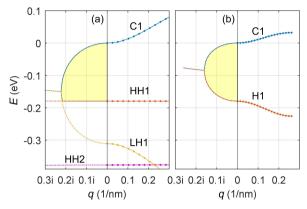

Fig. 1. Dispersion relation (energy E *vs.* Bloch wavevector q) in the growth direction of 3.2/3.2 nm InAs/GaSb SL calculated using a 4-band **k·p** Hamiltonian with parameters taken from Ref. 35 (a), 6/6 nm InAs/GaSb SL calculated using the 2-band Hamiltonian of (1) with parameter $E_p = 19$ eV adjusted such as to keep the same values of electron effective masses (b): $m_e = 0.022/0.042$ for InAs/GaSb, in both models. Filled areas show the integral of action, which determines the btb tunnelling current in both models

When studying btb tunnelling transitions, attention should be paid on the imaginary branch of dispersion; the tunnelling current exponentially depends on the area of the region enclosed by an imaginary branch connecting the real band extremes, i.e., the action integrals [36, 37]. As can be seen, this area is smaller for the 2-band model, so its use would provide overestimated btb tunnelling currents. It can be also seen that, for the 4-band case, the imaginary branch connecting C1-H1 extremes is determined not only by HH1 and C1 bands but also by the first light-hole (LH1) miniband. Therefore, to verify the hypothesis of a significant reduction of btb tunnelling current in SL devices, a multiband (at least 4-band) Hamiltonian would be more appropriate, which is left for future investigations.

2. Model and method

The device is modelled with the two-band Hamiltonian [38, 39]

$$H = \begin{bmatrix} E_c(z,k) & \hbar\sqrt{\dfrac{E_p}{2m_0}}\dfrac{\partial}{\partial z} \\[3mm] -\hbar\sqrt{\dfrac{E_p}{2m_0}}\dfrac{\partial}{\partial z} & E_\upsilon(z,k) \end{bmatrix}, \qquad (2)$$

in which the band edge energies are corrected for the in-plane kinetic energy, i.e., $E_{c,\upsilon}(z,k) = E_{c,\upsilon}(z) \pm \hbar^2 k^2/2m_{\parallel c,\upsilon}$, where $k = k_\parallel$ is the in-plane momentum modulus, and z is

the growth direction. The coupling of bands is described by the value of the Kane parameter, $E_p = 19$ eV, identical for both materials. Calculations were made for a p-i-n diode made of $9 \times (6$ nm-InAs/6 nm-GaSb) SL periods. As already mentioned, the widths of SL layers were adjusted to match up the resulting C1-H1 gap with the typical bandgaps of mid-IR SL-based devices. It is, however, important to point out that the actual bandgap of 6/6 nm InAs/GaSb SL is close to the estimate provided by the 4-band $\mathbf{k \cdot p}$ model, $E_g = E_{C1\text{-}HH1} \cong 47$ meV.

The SL was terminated with bulk n-InAs and p-GaSb materials, which extend to $\pm$ infinity. Attaching such 'leads' to the structure is necessary as electronic transport is possible only in *open* quantum system [6]. In order to reproduce the operating conditions of the absorber, the leads and the parts of the SL region, adjacent to them, were doped to $N_A = N_D = 1 \cdot 10^{18}$ cm^{-3}. The band diagram of the simulated device is shown in Fig. 2.
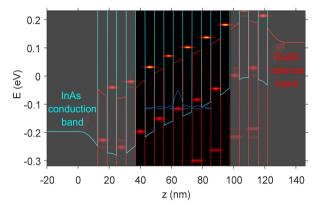

Fig. 2. Band diagram of the p-i-n SL device imposed onto the built-in potential. Doped regions are textured. The 2D colour map illustrates the local density of states for the vanishing in-plane momentum, $k = 0$. Short horizontal scars in the map emerge at energies of the Wannier-Stark (WS) states. Their spatial extend corresponds to the lengths of the scars, while their colour intensity to the densities of states magnitude. Dashed line is drawn at the energy of one of the WS states. The attached solid line shows DOS at this energy.

The equations of the NEGF formalism can be written in the matrix form [6]

$$(E\mathbf{I} - \mathbf{H} - \mathbf{\Sigma}_{\text{lead}}^R - \mathbf{\Sigma}_{\text{scatt}}^R)\mathbf{G}^R = \mathbf{I}$$
$$\mathbf{G}^< = \mathbf{G}^R(\mathbf{\Sigma}_{\text{lead}}^< + \mathbf{\Sigma}_{\text{scatt}}^<)\mathbf{G}^{R\dagger}$$
$$\mathbf{G}^> = \mathbf{G}^R - \mathbf{G}^{R\dagger} + \mathbf{G}^<$$
$$\mathbf{\Sigma}_{\text{scatt}}^< = \mathbf{\Sigma}_{\text{scatt}}^<(\mathbf{G}^R, \mathbf{G}^>),$$

(3)

useful for numerical solutions in real space. In (3), $\mathbf{I}$ is the unity matrix, $\dagger$ is the Hermitian operator, and $\mathbf{\Sigma}$'s and $\mathbf{G}$'s are self-energy and the Green's function (GF) matrices, respectively. They have the structure imposed by the structure of the Hamiltonian matrix

$$\mathbf{H} = \begin{bmatrix} \mathbf{H}_{cc} & \mathbf{H}_{cv} \\ \mathbf{H}_{vc} & \mathbf{H}_{vv} \end{bmatrix},$$

(4)

$$\mathbf{G} = \begin{bmatrix} \mathbf{G}_{cc} & \mathbf{G}_{cv} \\ \mathbf{G}_{vc} & \mathbf{G}_{vv} \end{bmatrix},$$

(5)

$$\mathbf{\Sigma} = \begin{bmatrix} \mathbf{\Sigma}_{cc} & \mathbf{\Sigma}_{cv} \\ \mathbf{\Sigma}_{vc} & \mathbf{\Sigma}_{vv} \end{bmatrix}.$$

(6)

The size of the matrices is determined by the size of a device Hamiltonian, i.e., $\mathbf{H} = \mathbf{H_D}$, because in the NEGF formalism the interaction with semi-infinite leads can be accounted for by smart self-energies $\mathbf{\Sigma}_{\text{lead}}$ added to the device Hamiltonian [6]. In the authors' approach, these self-energies are the single-value complex numbers, which enter the first and last diagonal element of $\mathbf{\Sigma}_{cc}$ [40]. On the contrary, $\mathbf{\Sigma}_{\text{scatt}}$ is a full matrix. It is the sum of $\mathbf{\Sigma}_{\text{phon}}$ and $\mathbf{\Sigma}_{\text{IR}}$ – the matrices related to scattering processes; namely, the scattering caused by phonons, both optical and acoustic, and the scattering caused by the interface roughness (IR). The formulations for the elements of the self-energy matrices $\mathbf{\Sigma}_{\text{phon}}$, $\mathbf{\Sigma}_{\text{IR}}$ were adapted from Ref. 9. It should be noted that phonon scattering was not limited to the intra-band process, but also accounts for inter-band transitions; however, only when bands are separated by less than LO-phonon energy, $E_{\text{LO}} = 30$ meV. Other inter-band processes, like Shockley-Read-Hall, Auger, and radiative recombination were not included in the calculations.

The NEGF equations were solved self-consistently with the Poisson's equation. Establishing the latter got into some problems as, in a T2SL structure, free carriers above/below the band edge cannot be always considered as carrying negative/positive electric charge. This issue was solved by defining the *virtual band edge* localized (in E-z space) in the middle between H1 and C1 minibands.

The band diagram in Fig. 2 is imposed onto the built-in potential, which was evaluated for the unbiased device. The observed band bending (resulting from the doping strategy) made the whole-contact terminations used in the model carrier-selective (p/n-type lead may only feed H1/C1 minibands), which is crucial for the photovoltaic operation [41]. This functionality makes these terminations a reasonable model of the contact region in a real device.

It follows from (2) and (3) that the GF matrices are functions of two parameters, i.e., the total energy E and the in-plane momentum modulus k; $\mathbf{G} = \mathbf{G}(E, k)$. The DOS, densities of electrons (DOE), and currents, which are related to the elements of $\mathbf{G}$'s [20, 34] are then the energy-momentum-resolved quantities. For example, in Fig. 2, the local DOS at $k = 0$ is shown as a function of the total energy E. It is clear that in the central part of the device, the built-in field breaks the minibands into the ladder of the localised WS states [42]. It can be also observed that the built-in field makes the H1 and C1 minibands cross, which is necessary for the btb tunnelling. This situation resembles well the situation in real devices (with a much lower built-in field), in which Zener tunnelling is likely to occur under a large reverse bias.

3. Results

3.1. Inter-band quantum tunnelling

As demonstrated in Fig. 2, at the sufficiently high electric field F, the minibands break into WS states. They act as resonant centres for the btb tunnelling process; each time the WS state in the conduction band aligns energetically with the WS state in the valence band, the

tunnelling current is enhanced. The effect was observed as oscillations in the current-voltage characteristics in devices made of high-quality materials, in which defect-assisted tunnelling did not hide the direct btb tunnelling current [43–47]. The authors' simulations presented in Fig. 3 confirm the oscillatory structure of the *I-V* curve.
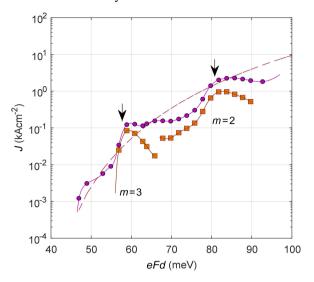

Fig. 3. Current-voltage (*I-V*) characteristics calculated with the NEGF method for the reverse-biased T2SL p-i-n diode (lines+symbols). Arrows indicate the position of resonances, calculated with (7) for *m* = 2 and *m* = 3. Data series correspond to: circles – total current, squares – individual btb transition between WS states. Line with no symbols depicts *I-V* characteristics calculated with the Wentzel-Kramers-Brillouin (WKB) method for the virtual bulk material with effective parameters: $E_g = 0.17$, $m_c = m_{C1} = 0.026$, $m_v = m_{H1} = 0.0173$.

The maxima of the current coincide with the resonance condition

$$eF\left(m + \frac{1}{2}\right)d = E_g, \qquad (7)$$

where *d* is the SL period, E_g is the C1-H1 bandgap, and $m + 1/2$ is the number of SL periods spanned by the tunnelling process. Number *m* can be identified not only from the position of current maxima in Fig. 3, but also

directly from the spatially resolved current spectrum like that presented in Fig. 4(c).

Fixing the position (*z*) and limiting the integration to a certain energy window, individual btb transitions can be studied. The data series labelled *m* = 2 and *m* = 3 in Fig. 3 correspond to the transitions between the WS states, which are separated by *m* + 1/2 lattice periods. They are observed in different ranges of the electric field. The *z*-resolved current spectrum in Fig. 4(c) was calculated for a field of ≈81 kV/cm, which maximizes the current for *m* = 2. The maxima of individual btb transitions occur when the WS states in conduction and valence bands align for the vanishing in-plane momentum. In this case, the barriers for the tunnelling process are the lowest. As $E(k)$ dispersions for the H1 and C1 minibands have opposite curvatures, the alignment of the states may also take place for non-zero *k*-values. In this case, the barriers for the tunnelling process increase by the sum of the in-plane energies $\hbar^2 k^2/2m_{\|v} + \hbar^2 k^2/2m_{\|c}$, which makes the transmission coefficient decrease exponentially with k^2 increasing. Consequently, the right-hand slope of the current spectrum for an individual transition decreases exponentially. For the same reason, transitions at higher *k*, e.g., at $k^2 \cong 0.06$ nm^{-2} and 0.12 nm^{-2}, are invisible in the momentum-resolved current density spectrum in Fig. 4(d). This scenario applies only to fields larger than the field that maximizes the inter-band current (makes the WS states align for *k* = 0), as only in this case the WS sub-bands may cross. For lower fields (voltages), the sub-bands do not cross for any (real) *k*, so a direct btb transition is impossible. The phonon-assisted tunnelling is still possible, provided that the gap between the WS sub-bands is less than the LO-phonon energy. This effect tempers the left-hand cut-off of the current spectrum of an individual transition. All these issues are illustrated in Figs. 3 and 4.

3.2. Virtual material approximation

In simplified drift-diffusion (DD) approaches, the SL material is often replaced with some equivalent (bulk) material that has parameters derived from SL properties [48–51]. Namely, its bandgap is defined as the energy difference between the lower edge of miniband C1 and the
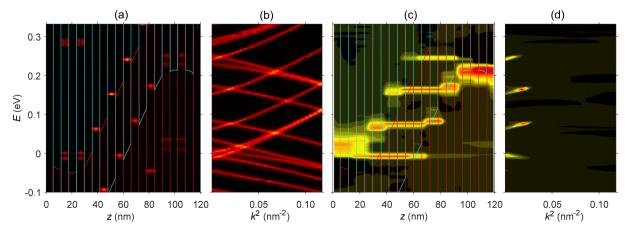

Fig. 4. Band diagram and DOS for the vanishing in-plane momentum *k* = 0, for the device reverse-biased to *U* = −0.235 V (a). Spatially-averaged DOS as the function of k^2; brighter lines show the hole and electron sub-bands formed by the WS states (b). The *z*-resolved energetic spectrum of the total current density (c). Momentum-energy-resolved current density at *z* = 63 nm (device centre) (d); current flows at *k* for which WS sub-bands of electrons and holes in (b) cross; transitions for subbands crossing at large *k*-values are invisible because respective currents are much lower (due to higher barriers).

upper edge of miniband H1, while the effective masses are calculated from the curvature of the dispersion relation in the minibands as $m_{c/\upsilon} = m_{C1/H1} = \hbar^2/[2\partial E(q)/\partial q^2|_{q=0}]$. For the cosine dispersion relation, $E(q) = \frac{1}{2}W[1 - \cos(qd)]$, valid approximately for the minibands (in the growth direction), the masses can be further related to miniband widths, $W_{C1/H1}$. Namely, $m_{C1/H1} = 2\hbar^2/(d^2 W_{C1/H1})$.

For the SL under consideration, the values of 'virtual' material parameters, $E_g = 0.17$ eV and $m_{c/\upsilon} = 0.026/0.0173$, were evaluated from the simulation performed for the conditions that flatten the minibands so that their widths can be easily read out (see Fig. 5). This can be achieved, e.g., by dismissing the need of self-consistency with the Poisson's equation.
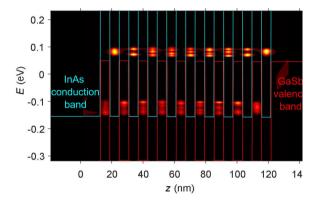

Fig. 5. Band diagram of the p-i-n SL without built-in potential. The 2D colour map depicts the local DOS for vanishing in-plane momentum, $k = 0$. The widths of the minibands: $W_{C1} = 0.04$ eV, $W_{H1} = 0.06$ eV and bandgap $E_{C1\text{-}H1} = 0.17$ eV have been read out from this plot.

The btb tunnelling current can be calculated as [36]

$$J_{BTB} = \frac{e}{\pi \hbar} \int \frac{d^2 k}{(2\pi)^2} \int dE [f_L(E) - f_R(E)] T(E,k), \quad (8)$$

where $f_{L,R}$ are the Fermi factors in the leads, and the integration is limited to the range of energies, for which the virtual bands cross. Equation (1) for the transmission coefficient is valid only for the constant electrical field. When the field is non-uniform, the coefficient T can be calculated in the WKB approximation from the action integral [2, 36]

$$T(E,k) = \exp\left(-2 \int_{z_1(E,k)}^{z_2(E,k)} \kappa(E,k,z) dz\right), \quad (9)$$

where z_1, z_2 are the classical turning points, and $i\kappa$ is the solution of the eigenvalue problem in the forbidden gap. For the band structures, in which the electrons and holes have different effective masses (the case here), the simple two-band Hamiltonian of (2) may not be sufficient. In this case, the integration over the complex band needs to be divided into two elliptic branches [37]

$$\int_{z_1}^{z_2} \kappa dz = \int_{z_1}^{z_q} \kappa_1 dz + \int_{z_q}^{z_2} \kappa_2 dz, \quad (10)$$

which join in the branch point z_q. It is defined in such a way that,

$$E - E_\upsilon(z_q, k) = E_q \equiv E_g \frac{m_c}{m_c + m_\upsilon}. \quad (11)$$

For electrons travelling toward a negative direction (the case here – see Fig. 2)

$$\kappa_1 = \frac{1}{\hbar} \sqrt{2m_c m_0 (E_c - E)[1 - (E_c - E)/(2E_g - 2E_q)]}, \quad (12)$$

$$\kappa_2 = \frac{1}{\hbar} \sqrt{2m_\upsilon m_0 (E - E_\upsilon)[1 - (E - E_\upsilon)/(2E_q)]}, \quad (13)$$

where both band edges, E_c and E_υ, are the functions of position z and momentum modulus k. The results of these calculations have been included in Fig. 3. In general, the WKB approximation agrees well with quantum calculations in the sense that the differences are within an order of magnitude. As expected, there are no features on the I-V curve because the WKB approximation assumes tunnelling between the continuous domains of electronic states whereas, as shown in Fig. 4(d), in a superlattice, the btb transitions occur only at certain points of the E-k space.

4. Conclusions

Theoretical issues related to electrical transport in T2SL devices in many aspects need to be solved with the use of quantum methods. One of them is the inter-band tunnelling because, in general, the DD approach cannot account for this quantum phenomenon. The analysis made by means of the NEGF method performed in this paper reveals that a direct btb tunnelling in T2SL devices is very different from that in bulk devices. The difference mainly concerns the number of states, available for the tunnelling event. Their population is described by the overlap of DOSs on both sides of the tunnelling transition. In bulk devices, there are plenty of such states; they fill the whole range of energies in which the bands on the opposite side of the junction cross. In an SL material, there are few of such states; their number equals the number of electronic WS sub-bands on the n-side of the junction that cross hole-WS sub-bands on the opposite p-side of the junction (see Fig. 4). Due to the above difference, semi-classical approximations usually employed to estimate the btb tunnelling current in the bulk junction, for SL devices, can only be used for an 'order of magnitude' approximation.

To put the work in a proper context, one needs to mention that electronic transport in SL-based devices, used in mid-IR applications, can be also influenced by inter-band currents other than direct btb tunnelling. Of these, the trap-assisted tunnelling is the most important. In particular, this current may dominate over btb current in the SL devices doped below $1 \cdot 10^{17}$ cm^{-3} [48]. So, the oscillations in the current-voltage characteristics predicted by the analyses performed in this paper can be observed only in the devices made of high-quality materials, in which the trap-mediated tunnelling components are lower than the direct btb component [43–47].

Acknowledgements

References

[1] Rogalski, A., Martyniuk, P. & Kopytko, M. InAs/GaSb type-II superlattice infrared detectors: Future prospect. *Appl. Phys. Rev.* **4**, 031304 (2017). https://doi.org/10.1063/1.4999077

[2] Sze, S. M. & Ng, K. K. *Physics of Semiconductor Devices*. *3rd Edition* (John Wiley & Sons, 2007).

[3] Yang, Q. K., Fuchs, F., Schmitz, J. & Pletschen, W. Investigation of trap-assisted tunneling current in InAs/(GaIn) Sb superlattice long-wavelength photodiodes. *Appl. Phys. Lett.* **81**, 4757–4759 (2002). https://doi.org/10.1063/1.1529306

[4] Martyniuk, P. *et al*. Modeling of midwavelength infrared InAs/GaSb type II superlattice detectors. *Opt. Eng.* **52**, 061307 (2013). https://doi.org/10.1117/1.OE.52.6.061307

[5] Aifer, E. H. *et al*. W-structured type-II superlattice-based long-and very long wavelength infrared photodiodes. *Proc. SPIE* **5732**, 259–272 (2005). https://doi.org/10.1117/12.597134

[6] Datta, S. *Electronic Transport in Mesoscopic Systems*. (Cambridge University Press, 1997).

[7] Keldysh, L. V. Diagram technique for nonequilibrium processes. *Sov. Phys. JETP* **20**, 1018–1026 (1965). http://jetp.ras.ru/cgi-bin/dn/e_020_04_1018.pdf

[8] Kadanoff, L. P. & Baym, G. *Quantum Statistical Mechanics: Green's Function Methods in Equilibrium and Nonequilibrium Problems* (CRC Press, Boca Raton. 2019). https://doi.org/10.1201/9780429493218

[9] Lake, R., Klimeck, G., Bowen, R. C. & Jovanovic, D. Single and multiband modeling of quantum electron transport through layered semiconductor devices. *J. Appl. Phys.* **81**, 7845–7869 (1997). https://doi.org/10.1063/1.365394

[10] Bowen, R. C., Klimeck, G. & Lake, R. K. Quantitative simulation of a resonant tunneling diode. *J. Appl. Phys.* **81**, 3207–3213 (1997). https://doi.org/10.1063/1.364151

[11] Wang, J., Polizzi, E. & Lundstrom, M. A three-dimensional quantum simulation of silicon nanowire transistors with the effective-mass approximation. *J. Appl. Phys.* **96**, 2192–2203 (2004). https://doi.org/10.1063/1.1769089

[12] Luisier, M. & Klimeck, G. Simulation of nanowire tunneling transistors: From the Wentzel–Kramers–Brillouin approximation to full-band phonon-assisted tunneling. *J. Appl. Phys.* **107**, 084507 (2010). https://doi.org/10.1063/1.3386521

[13] Pourfath, M. & Kosina, H. Computational study of carbon-based electronics. *J. Comput. Electron.* **8**, 427–440 (2009). https://doi.org/10.1007/s10825-009-0285-z

[14] Steiger, S., Veprek, R. G. & Witzigmann, B. Electroluminescence From a Quantum-Well LED Using NEGF. in *2009 13th International Workshop on Computational Electronics* 1–4 (IEEE 2009). http://doi.org/10.1109/IWCE.2009.5091112

[15] Shedbalkar, A., Andreev, Z. & Witzigmann, B. Simulation of an indium gallium nitride quantum well light-emitting diode with the non-equilibrium Green's function method. *Phys. Status Solidi B* **253**, 158–163 (2016). https://doi.org/10.1002/pssb.201552276

[16] Wang, R. *et al*. Quantum mechanical modeling the emission pattern and polarization of nanoscale light emitting diodes. *Nanoscale* **8**, 13168–13173 (2016). https://doi.org/10.1039/C6NR02356H

[17] Henrickson, L. E. Nonequilibrium photocurrent modeling in resonant tunneling photodetectors. *J. Appl. Phys.* **91**, 6273–6281 (2002). https://doi.org/10.1063/1.1473677

[18] Akhavan, N. D. *et al*. Superlattice barrier HgCdTe nBn infrared photodetectors: Validation of the effective mass approximation. *IEEE Trans. Electron Devices* **63**, 4811–4818 (2016). http://doi.org/10.1109/TED.2016.2614677

[19] Naser, M. A., Deen, M. J. & Thompson, D. A. Photocurrent modeling and detectivity optimization in a resonant-tunneling quantum-dot infrared photodetector. *IEEE J. Quantum Electron.* **46**, 849–859 (2010). http://doi.org/10.1109/JQE.2010.2040245

[20] Aeberhard, U. & Morf, R. H. Microscopic nonequilibrium theory of quantum well solar cells. *Phys. Rev. B* **77**, 125343 (2008). https://doi.org/10.1103/PhysRevB.77.125343

[21] Aeberhard, U. Simulation of ultrathin solar cells beyond the limits of the semiclassical bulk picture. *IEEE J. Photovolt.* **6**, 654–660 (2016). http://doi.org/10.1109/JPHOTOV.2016.2528405

[22] Cavassilas, N., Michelini, F. & Bescond, M. Modeling of nanoscale solar cells: The Green's function formalism. *J. Renew. Sustain. Energy* **6**, 011203 (2014). https://doi.org/10.1063/1.4828366

[23] Kubis, T. *et al*. Theory of nonequilibrium quantum transport and energy dissipation in terahertz quantum cascade lasers. *Phys. Rev. B* **79**, 195323 (2009). https://doi.org/10.1103/PhysRevB.79.195323

[24] Lee, S. C. & Wacker, A. Nonequilibrium Green's function theory for transport and gain properties of quantum cascade structures. *Phys. Rev. B* **66**, 245314 (2002). https://doi.org/10.1103/PhysRevB.66.245314

[25] Hałdaś, G., Kolek, A. & Tralle, I. Modeling of mid-infrared quantum cascade laser by means of nonequilibrium Green's functions. *IEEE J. Quantum Electron.* **47**, 878–885 (2011). http://doi.org/10.1109/JQE.2011.2130512

[26] Grange, T. Contrasting influence of charged impurities on transport and gain in terahertz quantum cascade lasers. *Phys. Rev. B* **92**, 241306(R) (2015). https://doi.org/10.1103/PhysRevB.92.241306

[27] Miloszewski, J. M. & Wartak, M. S. Semiconductor laser simulations using non-equilibrium Green's functions. *J. Appl. Phys.* **111**, 053104 (2012). https://doi.org/10.1063/1.3689324

[28] Grange, T. Electron transport in quantum wire superlattices. *Phys. Rev. B* **89**, 165310 (2014). https://doi.org/10.1103/PhysRevB.89.165310

[29] Bertazzi, F., Tibaldi, A., Goano, M., Montoya, J. A. G. & Bellotti, E. Nonequilibrium Green's function modeling of type-II superlattice detectors and its connection to semiclassical approaches. *Phys. Rev. Appl.* **14**, 014083 (2020). https://doi.org/10.1103/PhysRevApplied.14.014083

[30] Bellotti, E. *et al*. Disorder-induced degradation of vertical carrier transport in strain-balanced Antimony-based superlattices. *Phys. Rev. Appl.* **16**, 054028 (2021). https://doi.org/10.1103/PhysRevApplied.16.054028

[31] Aeberhard, U., Gonzalo, A. & Ulloa, J. M. Photocarrier extraction in GaAsSb/GaAsN type-II QW superlattice solar cells. *Appl. Phys. Lett.* **112**, 213904 (2018). https://doi.org/10.1063/1.5030625

[32] Ilatikhameneh, H., Salazar, R. B., Klimeck, G., Rahman, R. & Appenzeller, J. From Fowler-Nordheim to nonequilibrium Green's function modeling of tunneling. *IEEE Trans. Electron Devices* **63**, 2871–2878 (2016). http://doi.org/10.1109/TED.2016.2565582

[33] Tibaldi, A. *et al*. Modeling infrared superlattice photodetectors: From nonequilibrium Green's functions to quantum-corrected drift diffusion. *Phys. Rev. Appl.* **16**, 044024 (2021). https://doi.org/10.1103/PhysRevApplied.16.044024

[34] Aeberhard, U. Quantum-kinetic theory of photocurrent generation via direct and phonon-mediated optical transitions. *Phys. Rev. B* **84**, 035454 (2011). https://doi.org/10.1103/PhysRevB.84.035454

[35] Qiao, P.-F., Mou, S. & Chuang, S. L. Electronic band structures and optical properties of type-II superlattice photodetectors with interfacial effect. *Opt. Express* **20**, 2319–2334 (2012). https://doi.org/10.1364/OE.20.002319

[36] Pan, A. & Chui, C. O. Modeling direct interband tunneling. I. Bulk semiconductors. *J. Appl. Phys.* **116**, 054508 (2014). https://doi.org/10.1063/1.4891527

[37] Guan, X., Kim, D., Saraswat, K. C. & Wong, H. S. P. Complex band structures: From parabolic to elliptic approximation. *IEEE Electron. Device Lett.* **32**, 1296–1298 (2011). http://doi.org/10.1109/LED.2011.2160143

[38] Leavitt, R. P. Empirical two-band model for quantum wells and superlattices in an electric field. *Phys. Rev. B* **44**, 11270 (1991). https://doi.org/10.1103/PhysRevB.44.11270

[39] Sirtori, C., Capasso, F., Faist, J. & Scandolo, S. Nonparabolicity and a sum rule associated with bound-to-bound and bound-to-continuum intersubband transitions in quantum wells. *Phys. Rev. B* **50**, 8663 (1994). https://doi.org/10.1103/PhysRevB.50.8663

[40] Kolek, A. Nonequilibrium Green's function formulation of intersubband absorption for nonparabolic single-band effective mass Hamiltonian. *Appl. Phys. Lett.* **106**, 181102 (2015). https://doi.org/10.1063/1.4919762

[41] Würfel, P. & Würfel, U. *Physics of Solar Cells: From Basic Principles to Advanced Concepts* (John Wiley & Sons, 2016).

[42] Wacker, A. Semiconductor superlattices: a model system for nonlinear transport. *Phys. Rep.* **357**, 1–111 (2002). https://doi.org/10.1016/S0370-1573(01)00029-1

[43] Bürkle, L., Fuchs, F., Ahlswede, E., Pletschen, W. & Schmitz, J. Wannier-Stark localization in InAs/(GaIn) Sb superlattice diodes. *Phys. Rev. B* **64**, 045315 (2001). https://doi.org/10.1103/PhysRevB.64.045315

[44] Hamaguchi, C. *et al*. Wannier-Stark localization in superlattices. *Jpn J. Appl. Phys.* **34**, 4519 (1995). https://doi.org/10.1143/JJAP.34.4519

[45] Nguyen, B. M., Hoffman, D., Huang, E. K. W., Delaunay, P. Y. & Razeghi, M. Background limited long wavelength infrared type-II InAs/GaSb superlattice photodiodes operating at 110 K. *Appl. Phys. Lett.* **93**, 123502 (2008). https://doi.org/10.1063/1.2978330

[46] Wei, Y. *et al*. Uncooled operation of type-II InAs/GaSb superlattice photodiodes in the midwavelength infrared range. *Appl. Phys. Lett.* **86**, 233106 (2005). https://doi.org/10.1063/1.1947908

[47] Kazemi, A. *et al*. Mid-wavelength infrared unipolar nBp superlattice photodetector. *Infrared Phys. Technol.* **88**, 114–118 (2018). https://doi.org/10.1016/j.infrared.2017.11.008

[48] Delmas, M. *et al*. Identification of a limiting mechanism in GaSb-rich superlattice midwave infrared detector. *J. Appl. Phys.* **119**, 174503 (2016). https://doi.org/10.1063/1.4948670

[49] Fuchs, F. *et al*. Magneto-optics of InAs/Ga$_{1-x}$In$_x$Sb infrared superlattice diodes. *Appl. Phys. Lett.* **73**, 3760–3762 (1998). https://doi.org/10.1063/1.122886

[50] Martyniuk, P. *et al*. Modeling of midwavelength infrared InAs/GaSb type II superlattice detectors. *Opt. Eng.* **52**, 061307 (2013). https://doi.org/10.1117/1.OE.52.6.061307

[51] Szmulowicz, F., Haugan, H. J. & Brown, G. J. Analysis of (110) indium arsenide–gallium antimonide superlattices for infrared detection. *J. Appl. Phys.* **104**, 074505 (2008). https://doi.org/10.1063/1.2990003